PERGAMON

International Journal of Multiphase Flow 25 (1999) 795–812

International Journal of Multiphase Flow

www.elsevier.com/locate/ijmulflow

Averaged and time-dependent characteristics of the motion of an elongated bubble in a vertical pipe

S. Polonsky, D. Barnea, L. Shemer *

Department of Fluid Mechanics and Heat Transfer, Faculty of Engineering, Tel-Aviv University, Tel-Aviv 69978, Israel

Received 30 November 1997; received in revised form 20 October 1998

Abstract

The motion of elongated (Taylor) bubbles in air–water vertical flow is studied by processing consecutive series of digitized video images. The shape of the elongated bubbles, as well as the velocities of the liquid–gas interfaces, are measured for various flow conditions. The bubble velocity variation caused by air expansion under the influence of hydrostatic pressure gradient is measured and compared with model predictions. An oscillatory motion of the bubble bottom is observed. The frequency and the amplitude of these oscillations are studied as a function of bubble length and water flow rate. This information is essential for accurate modeling of developing gas–liquid slug flow. © 1999 Elsevier Science Ltd. All rights reserved.

Keywords: Two-phase slug flow; Image processing

1. Introduction

Slug flow occurs over a wide range of parameters in gas–liquid pipe flow. It is characterized by a quasi-periodic alteration of liquid slugs and long bullet-shaped bubbles. In vertical pipes, elongated bubbles have a rounded cup, while the tail is generally assumed to be nearly flat. The liquid around the bubbles moves as a thin falling film. Each liquid slug sheds liquid in its back to the subsequent film, which is then injected into the bubble wake as a circular wall jet, producing a mixing zone in the bubble wake which has a shape of a toroidal vortex.

The motion of a single elongated bubble in liquid flow is a basic phenomenon in slug flow. The rise of a single bubble in stagnant and moving liquid in a vertical pipe has been studied by numerous researchers, both theoretically (Dumitrescu, 1943; Davies and Taylor, 1949;

* Corresponding author.

PII: S0301-9322(98)00066-4

Goldsmith and Mason, 1962; Collins et al., 1978; Mao and Dukler, 1990) and experimentally (White and Beardmore, 1962; Zukoski, 1966; Mao and Dukler, 1991). However, most of the data are related to the flow around the nose of the bubble. The calculations of the translational velocity of the elongated bubble are based on the estimated flow field in the front of the bubble.

For a fully developed slug flow, the distance between any two consecutive bubbles is large enough so that the trailing bubble is uninfluenced by the wake of the leading one. In this case, the information on the bubble nose motion is sufficient for the description of the flow. However, in the entrance region of the pipe, the distance between the bubbles is not sufficiently large. The bubbles in this region are influenced by flow in the wake of their predecessors, resulting in merging of bubbles and variation of the flow structure along the pipe (Moissis and Griffith, 1962; Taitel and Barnea, 1990). In order to model undeveloped and transient slug flow in entry regions as well as in terrain slugging observed in pipes of variable inclination, detailed knowledge of the flow field in the elongated bubble wake becomes essential.

The available information about the flow structure in the bubble wake is very limited. Moissis and Griffith (1962) measured the velocity profiles in the wake of a stationary plastic 'bubble'. This simulation has some shortcomings. The rigid boundary of the plastic model does not represent the free-surface boundary of the gas bubble. In addition, the flow conditions in their experiments are different from those in a real slug flow where the gas bubble moves relative to the pipe walls. Taitel et al. (1980) and Barnea and Brauner (1985) assumed that the minimum stable slug length corresponds to the distance at which the liquid film is absorbed by the slug. They viewed this process as a wall jet entering a large reservoir. The predicted stable slug length was in a good agreement with experimental results.

Kvernvold et al. (1984) used LDV-technique for measuring velocity profiles in the liquid slug and in the film region of a horizontal slug flow. Nakoryakov et al. (1989) performed a more extensive study of an instantaneous velocity field in a vertical flow using an electrochemical velocity probe. Radial and axial velocity profiles were obtained. They showed that the vortex ring in the mixing zone behind the Taylor bubble affects significantly the flow structure in the slug.

Shemer and Barnea (1987) performed a visualization study of velocity profiles behind the Taylor bubbles in vertical and horizontal slug flows using hydrogen bubble technique. They demonstrated the presence of two zones in the liquid slug: a mixing zone where the annular jet enters the slug, and a zone of a fully developed velocity profile. They concluded that the velocity of the elongated bubble is related to the value of the maximum instantaneous velocity in front of it.

Campos and Guedes de Carvalho (1988a, b) studied the shape of the elongated bubbles wake for various flow conditions using visualization technique. In their recent paper, Pinto and Campos (1996) studied the coalescence of pairs of gas bubbles rising in vertical columns of liquids covering a wide range of viscosities.

The present study is aimed at detailed experimental investigation of the motion of a single elongated bubble. Hydrodynamic parameters of the Taylor bubble, such as bubble shape, velocities of bubble nose and bottom, as well as bubble elongation due to hydrostatic pressure gradient, are measured. It is found that the bottom of the Taylor bubble undergoes quasi-periodic oscillations. The frequency spectra of these oscillations are measured for different flow

conditions. This information is essential for the investigation of the velocity field in the wake region behind the elongated bubble.

2. Experimental system and method

The experimental apparatus (Fig. 1) consists of an air and water supply system and a test section made of a vertical Perspex pipe 25 mm in diameter and about 170 diameters long. Filtered tap water flowing in a closed loop is used as a working fluid. The flow rate is regulated and measured by a set of Fisher–Porter rotameters. Air is supplied from a central

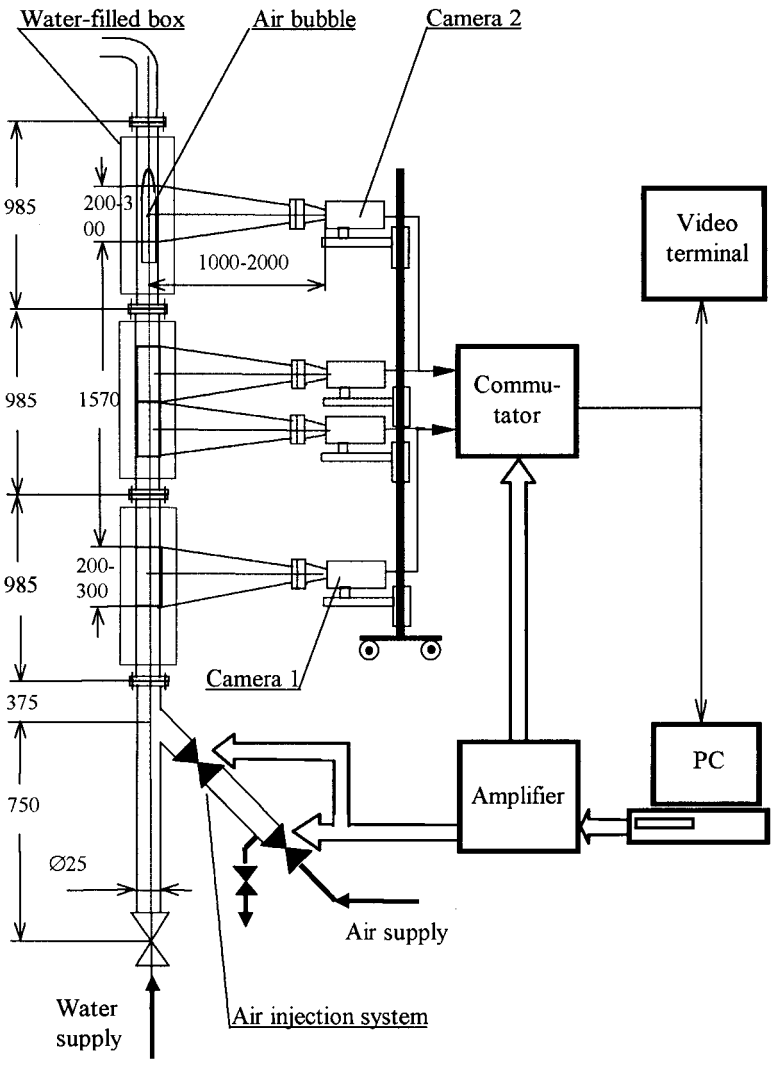

Fig. 1. Experimental facility.

compressed air line at the nominal pressure of 0.6 MPa. The 1 m long air inlet chamber is attached to the lower part of the test pipe at an angle of 30°. Individual bubbles are injected from this chamber, which is separated from the test pipe by a computer-controlled solenoid-activated ball valve. The valve, the chamber and the test section have the same inner diameter, in order to provide a smooth entrance of air bubbles. The pressure in the air chamber is accurately monitored. The length of the injected bubble is determined by the duration of the valve opening, which is controlled by the computer, as well as by the air pressure in the chamber. The test section is equipped with three rectangular transparent boxes filled with water. The boxes serve to reduce image distortion.

The movement of each elongated bubble is recorded consecutively at different axial locations by two interlaced NTSC video cameras attached to a vertical shaft. The exposure times of the cameras vary from 1/100 to 1/1000 s. The bubble can be illuminated by either a set of 500 W halogen lamps mounted on frames at opposite sides of the test section, or by a light sheet produced by a 5 W Argon ion laser. Video images are taken against a black background, so that the bubble appears as a white outline. In order to obtain a better spatial resolution in the vertical direction, the cameras are rotated by 90°, so that in the video images, the bubbles appear to move horizontally. In the course of experiments with the halogen lamps, tap water runs through the transparent boxes, cooling the test section against the heat from illumination, so that a constant temperature is maintained during the experiment. The boxes are equipped with ruler tapes providing length scale reference. During the experiments with the light sheet, a small amount (less than 0.01‰) of fluorescent dye is added to the water in the loop. The dye emits light when illuminated by a laser, thus selecting a vertical cross-section in the pipe which is about 1 mm thin and 1 m long.

The images of the bubble nose appear similar for both methods of illumination. The main difference between these two methods is the projection of the bubble bottom into the plane of view. When using halogen lamps, the bubble bottom is seen as a more or less regular ellipse. The ellipse branch corresponding to the far wall of the pipe may be obscured from view by the parts of the bubble closer to the camera. This makes the processing and interpretation of the images difficult. On the other hand, the light sheet produces the 2D cross-section of the bubble in the vertical plane through the pipe axis. The bubble bottom is projected into the plane of view as a simple curve which can easily be detected and interpreted. The disadvantage of the light sheet facility is that it can be easily implemented only at a certain location in the test section, while the halogen illumination permits to obtain images in any desired position along the pipe.

Two different arrangements of the cameras are used. In the first type of experiments, where the purpose is to examine the variation of the Taylor bubble parameters along the pipe, the two cameras are placed at the lower and the upper measurement stations, respectively (see Fig. 1). In this arrangement, halogen lamp illumination is used. When the purpose of the experiments is to study the temporal behavior of the Taylor bubble bottom, a continuous monitoring of the bubble motion over extensive time intervals is necessary. The two cameras in this case view the middle section of the test pipe, so that the fields of view of the cameras overlap slightly. In these experiments the pipe is illuminated in an axial cross-section by a vertical light sheet produced by the laser.

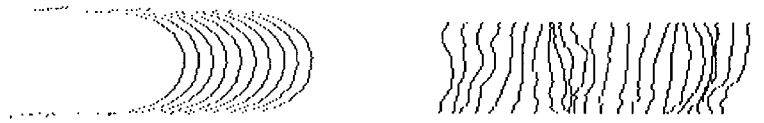

a) Nose outlines in a short image sequence

b) Bottom outlines in a short image sequence

Fig. 2. Bubble shape outlines

The output video signals of the two cameras are connected to a frame grabber board via a commutator box. The images at the rate of 30 frames/s are digitized and stored directly in the RAM of a personal computer and then transferred to a hard disk for permanent storage. In order to ensure the necessary synchronization between the various devices, e.g. the bubble injection, the switching between the cameras, and the recording process, they are all controlled by the clock of the same PC. The images are recorded only during the passage of the bubble through the field of view of the corresponding camera.

The eight bit (256 gray levels) video images have the size of 640×480 pixels. The image processing is performed on the same PC using software written especially for this purpose. First, the image of the pipe filled with water with no bubbles present is subtracted from each recorded frame. This procedure allows the uniformity and contrast of the images to be improved. The interlaced video images are then split into odd and even fields. The spacing between the lines is filled using linear interpolation between the gray levels in two adjacent lines. Hence, the effective rate of recording is 60 images/s. At the next stage of the processing, each image is enhanced by cleaning the background around the bubble in each frame, followed by noise reduction and edge enhancement (if necessary) (see e.g. Pratt, 1978). The bubble outline is found by an edge detection algorithm (separately for the bubble nose and the bubble bottom). Applying this procedure to each recorded frame, a sequence of 100–200 outlines of bubble shape is obtained for each moving bubble. An example of the recorded outlines of bubble nose and bubble bottom is presented in Fig. 2.

3. Experimental results

Experiments are carried out to study the instantaneous shape of a single elongated air bubble moving in a vertical pipe. Measurements are performed in stagnant and upward flowing liquid. The range of liquid flow velocities is 0–0.30 m/s. Bubbles with the length L from $L/D = 1$ to about $L/D = 20$, D being the pipe diameter, are studied. In stagnant liquid and in upward flow, all bubbles have a well-defined symmetrical shape with a spherical cup. The nose retains its shape while moving along the pipe (cf. Fig. 2). Contrary to that, the bottom of the Taylor bubble exhibits notable oscillations, and the shape of the bubble bottom varies as the bubble propagates along the pipe. The bubble bottom oscillations apparently are strongly dependent on the bubble length (Fig. 3).

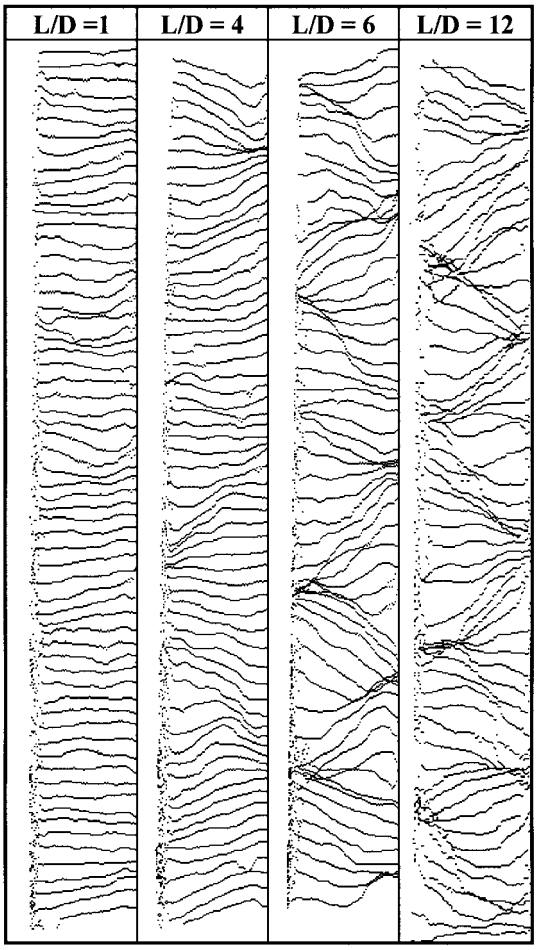

Fig. 3. The consecutive positions of the bubble bottom for different bubble lengths.

3.1. Averaged parameters

The results of Figs. 2 and 3 indicate that the bubble shape is time-dependent. The propagation velocity of the bubble nose at each radial location is calculated as the shift between nose profiles in different frames, divided by time elapsed between those frames. These values are first averaged over all radial positions, in order to obtain the averaged cross-sectional nose velocity and then averaged again for all images in the series. The propagation velocity of the bubble nose is calculated as a difference between the average tail positions in different frames, divided by the time elapsed between those frames, and averaged for all images in the series. The local instantaneous axial velocity on the tail interface is also calculated for different radial positions as a difference between the tail positions in adjacent frames.

The mean bubble parameters are thus computed from the consecutive images using the averaging expressions summarized in Table 1. The average shape of the bottom of the bubble (Fig. 4) was calculated based on all images of the corresponding series. Typically about 100–

Table 1
Averaging expressions

Nose profile in the jth image:
$x = x_N(i, j)$

Bottom profile in the jth image:
$x = x_B(i, j)$

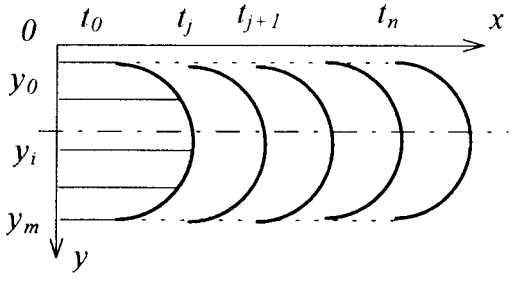

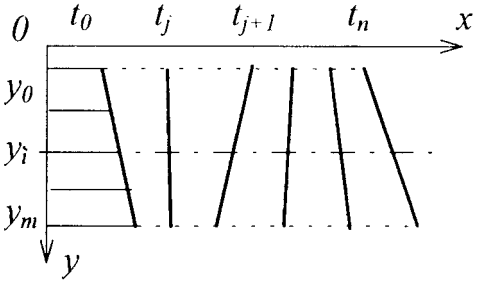

Local nose velocity:

$$U_N^k(i,j) = \frac{x_N(i,j+k) - x_N(i,j)}{k\Delta t}$$

Local bottom velocity:

$$U_B^k(i,j) = \frac{x_B(i,j+k) - x_B(i,j)}{k\Delta t}$$

Average nose velocity:

$$\bar{U}_N = \frac{\sum_{i=0}^{m}\sum_{j=0}^{n-k} U_N^k(i,j)}{(m+1)(n-k+1)}$$

Average bottom velocity:

$$\bar{U}_B = \frac{\sum_{i=0}^{m}\sum_{j=0}^{n-k} U_B^k(i,j)}{(m+1)(n-k+1)}$$

Instantaneous nose profiles in the frame of reference moving with the bubble:
$x'_N(i,j) = x_N(i,j) - \bar{U}_N t_j$

Instantaneous bottom profiles in the frame of reference moving with the bubble:
$x'_B(i,j) = x_B(i,j) - \bar{U}_B t_j$

Average nose shape

$$\bar{x}_N(i) = \frac{\sum_{j=0}^{n} x'_N(i,j)}{n+1}$$

Average bottom shape:

$$\bar{x}_B(i) = \frac{\sum_{j=0}^{n} x'_B(i,j)}{n+1}$$

Time-dependent nose tip position:
$X_N^{tip}(j) = \max_{i=0}^{m}[x_N(i,j)]$

Time-dependent average bottom position:
$X_B(j) = \sum_{i=0}^{m} x_B(i,j)/(m+1)$

Instantaneous bubble length: $L_b(j) = X_N^{tip}(j) - X_B(j)$
Average bubble length: $\bar{L}_b = \sum_{j=0}^{n} L_b(j)/(n+1)$
Fourier transform of time series of bottom location at the ith radial position:
$H_k(f_k, i) = \sum_{j=0}^{n} x'_B(i,j) e^{2\pi jk/(n+1)}$
Average power spectrum of bubble bottom oscillations: $\bar{P}_k(f_k) = \frac{1}{(n+1)^2}\sum_i |H_k|^2 (f_k, i)$
Total energy of bubble bottom oscillations: $E_{total} = \sum_k \bar{P}_k(f_k)$

200 individual bubble images are obtained for each injected Taylor bubble. The results are further averaged for 4–6 bubbles of nearly identical length. Fig. 4 clearly demonstrates that the bottom for all bubbles in stagnant water as well as in upward water flow has a typical concave shape. In spite of the fact that the instantaneous images of the bubble bottom are strongly dependent on the bubble length (Fig. 3), the averaged bubble bottom shape does not change notably with the length of the bubble (Fig. 4a). It also appears to be essentially insensitive to the liquid velocity in the pipe (Fig. 4b). The averaged radius of curvature of the bubble bottom is about 25 mm, i.e. about twice that of the bubble head.

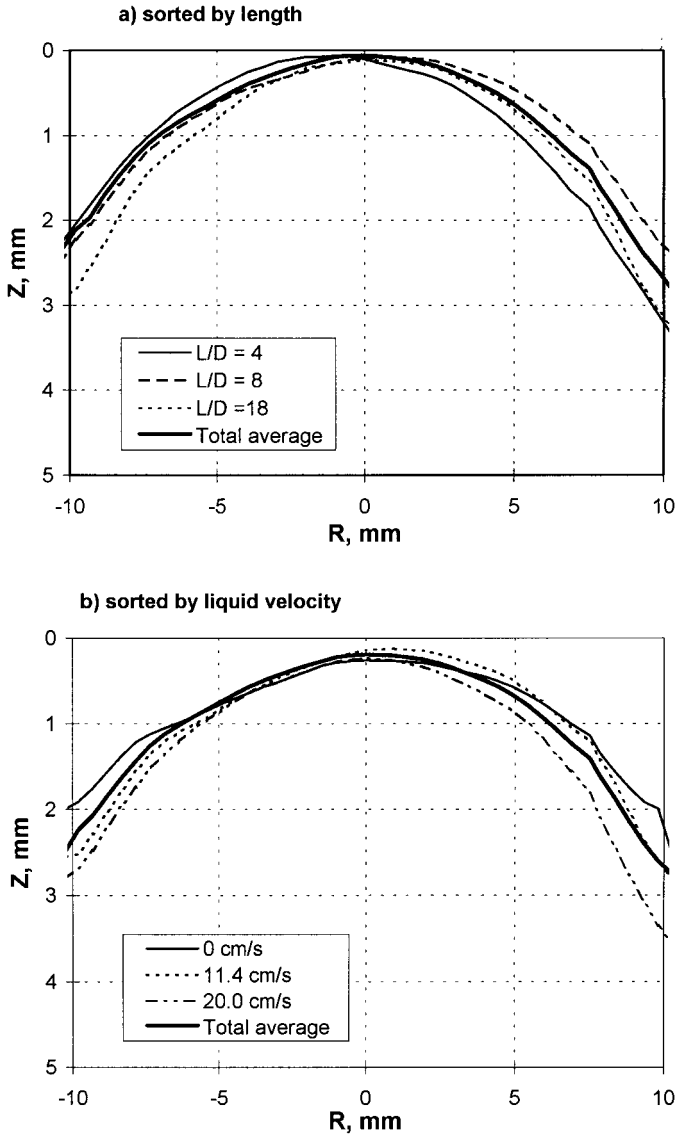

Fig. 4. Averaged bubble bottom shape: (a) sorted by bubble length; (b) sorted by liquid velocity.

The adopted technique allows the actual shape of the bubble to be determined quite precisely, and in particular, the variation of the film thickness δ along the bubble. In order to correct optical distortions due to pipe wall curvature, a ruler was inserted into the test section in the diameter plane of the pipe. The ruler was imaged by the camera, and the apparent distance between the counts in the image is used to calculate the distortion factor as a function of the radial position within the pipe. Measurements of the actual bubble profile are performed for a number of liquid velocities in the range from 0 to 27.7 cm/s. In Fig. 5 the measured bubble profile is shown for the two extreme values of the liquid flow rate. The film thickness at

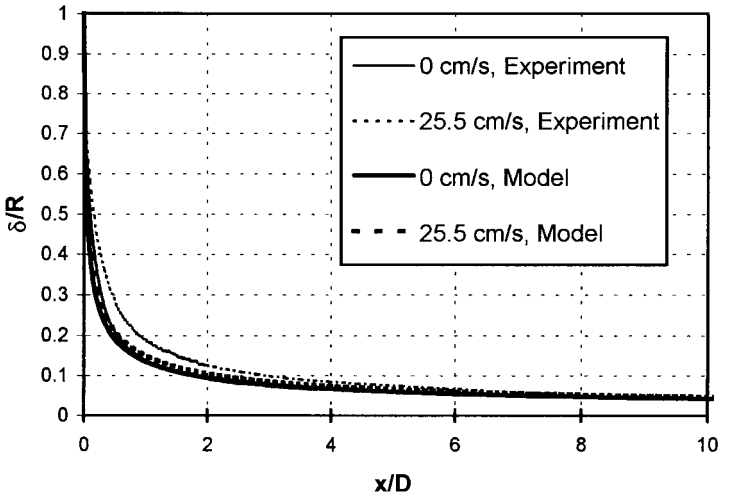

Fig. 5. Film thickness.

the bubble nose tends to increase with increasing liquid velocity. This effect is quite moderate and vanishes far from the bubble nose. Experiments, performed for bubbles of different lengths, also show that the bubble shape does not depend on the bubble length. In Fig. 5, the experimentally measured bubble outlines are compared with a simplified one-dimensional model (Barnea, 1990). In this model, the film thickness is calculated by a simultaneous solution of the liquid mass balance equation and the momentum equation for the liquid film in a frame of reference moving with the bubble. The agreement between the simplified one-dimensional model and the experiment is reasonable, although the model underpredicts the actual film thickness in the vicinity of the bubble nose.

The measured translational velocities of the Taylor bubble U_t (based on the bubble nose displacement) are presented in Fig. 6 for various bubble lengths and liquid flow rates. The solid

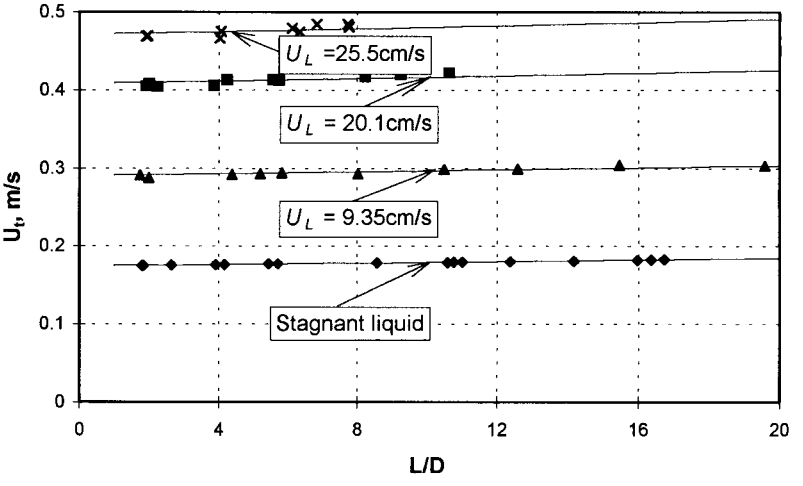

Fig. 6. Bubble nose velocities.

lines represent the linear best fit. These velocities increase with the liquid flow rate and appear to be slightly dependent on the bubble length due to the effect of gas compressibility. It is generally assumed that the translational velocity, U_t, can be expressed as (Nicklin et al., 1962)

$$U_t = CU_L + U_0 \tag{1}$$

where U_0 is the drift velocity, i.e. the Taylor bubble propagation velocity in stagnant liquid and U_L is the liquid velocity. The coefficient C in Eq. (1) represents the effect of the liquid velocity on the translational velocity of the Taylor bubble. It is generally assumed that the value of CU_L is equal to the maximum local liquid velocity in front of the nose tip (Nicklin et al., 1962; Nicklin, 1962; Collins et al., 1978). Thus, for turbulent pipe flow, $C \approx 1.2$, while for a fully developed laminar flow in a pipe the value of C approaches 2.

The drift velocity U_0 can be determined from the measured translational velocity in stagnant liquid in the limit of short bubbles, where the effects of compressibility vanish. This value is found to be $U_0 = 17.4$ cm/s, corresponding to $0.351\sqrt{gD}$, which is in agreement with Davies and Taylor (1949). Applying Eq. (1) for nonzero liquid flow rates with the value of $U_0 = 17.4$ cm/s allows the coefficient C to be calculated from the measured values of U_t in the limit of short bubbles. As expected, the values of C are found to depend on the liquid flow velocity, see Table 2. As the Reynolds number based on the liquid velocity, $Re_L = U_L D/\nu_L$ increases from 220 to 6380, the coefficient C decreases from 1.86 (which is close to the value usually assumed for laminar flow) to 1.16. This trend resembles the results obtained by Nicklin et al. (1962).

For all liquid flow rates employed here, the unperturbed flow is laminar, At the measurement station, located at $L = 2.5$ m from the entrance to the pipe, the flow is still undeveloped under most experimental condition ($L_{ent}/D = 0.06Re$; White, 1986). In the entrance region, the velocity profile is relatively flat, so that the ratio of the maximum to the mean velocity in the cross-section is considerably lower than 2. For low values of Re and correspondingly short entrance regions, the value of the coefficient C in Eq. (1) approaches the value of 2.

3.2. Effect of compressibility

The maximum absolute pressure variation in the experiments is less than 30%, so that the corresponding compressibility effects are quite weak. The present experimental techniques make it possible to distinguish between quite minor variations of the bubble length while it travels

Table 2

Flow velocity U_L (cm/s)	Re	L_{ent} (m)	L/L_{ent}	C
0.87	220	0.31	8.32	1.86
4.7	1800	1.70	1.52	1.66
9.35	2340	3.37	0.74	1.24
20.1	5030	7.24	0.36	1.17
25.5	6380	9.19	0.28	1.16

along the pipe. An effort therefore is made to extract quantitative information regarding the effect of gas compressibility on the bubble motion. Close analysis of the results presented in Fig. 6 reveals that the bubble propagation velocity U_t increases slightly with the bubble length. This effect can be attributed to the expansion of the bubble due to the hydrostatic pressure gradient while rising along the pipe. The expansion of the bubble indicates that the bubble nose velocity and the bubble tail velocity cannot be identical.

In order to investigate the effect of gas compressibility in detail, measurements of both bubble nose and bubble bottom velocities were performed along the central section of the pipe. The results are shown in Fig. 7a for the case of stagnant liquid, and in Fig. 7b for $U_L = 9.35$ cm/s. In both cases, the nose velocity is notably higher than that of the bottom; the difference between the two increases with the bubble length. Errors in the determination of the corresponding velocities from the recorded images are denoted by error bars. Note that due to vigorous oscillations of the bubble bottom, errors in the determination of the bubble bottom velocity are substantially larger than those of the bubble head. The observed variation of the velocities of the bubble nose and bottom with the bubble length can be explained on the basis of the following simple considerations.

Consider a bubble of mass m_G, volume V_G and density ρ_G, rising in a vertical pipe open from above. As a result of expansion of the gas in the bubble due to hydrostatic pressure gradient, an additional liquid velocity, u_L, is induced at the bubble front, which is related to the rate of bubble expansion:

$$u_L A = \frac{dV_G}{dt} = \frac{d}{dt}\left(\frac{m_G}{\rho_G}\right) = m_G \frac{d}{dt}\left(\frac{1}{\rho_G}\right) = -\frac{V_G}{\rho_G}\frac{d\rho_G}{dt} \tag{2}$$

where

$$V_G = \int_0^L \pi r^2(x)\,dx \tag{3}$$

$r(x)$ is the local radius of the bubble, L is the bubble length and x is the axial coordinate measured from the bubble nose. Eq. (1) for the velocity of the bubble nose, U_N is thus replaced by

$$U_N = C(U_L + u_L) + U_0 \tag{4}$$

According to ideal gas law,

$$\rho_G = \frac{P}{\mathcal{R}T} = \frac{P_a + \rho_L g h}{\mathcal{R}T} \tag{5}$$

$$\frac{d\rho_G}{dt} = \frac{\rho_L g}{\mathcal{R}T}\frac{dh}{dt} = -\frac{\rho_L g}{\mathcal{R}T}U_N \tag{6}$$

where P_a is the atmospheric pressure at the pipe outlet, h is the hydrostatic head in the pipe above the bubble and $\mathcal{R}$ is the air gas constant. Inserting Eqs. (3), (5) and (6) into Eq. (2) yields

$$u_L = U_N \frac{\int_0^L r^2(x)\,dx}{R^2\left(\frac{P_a}{\rho_L g} + h\right)} \tag{7}$$

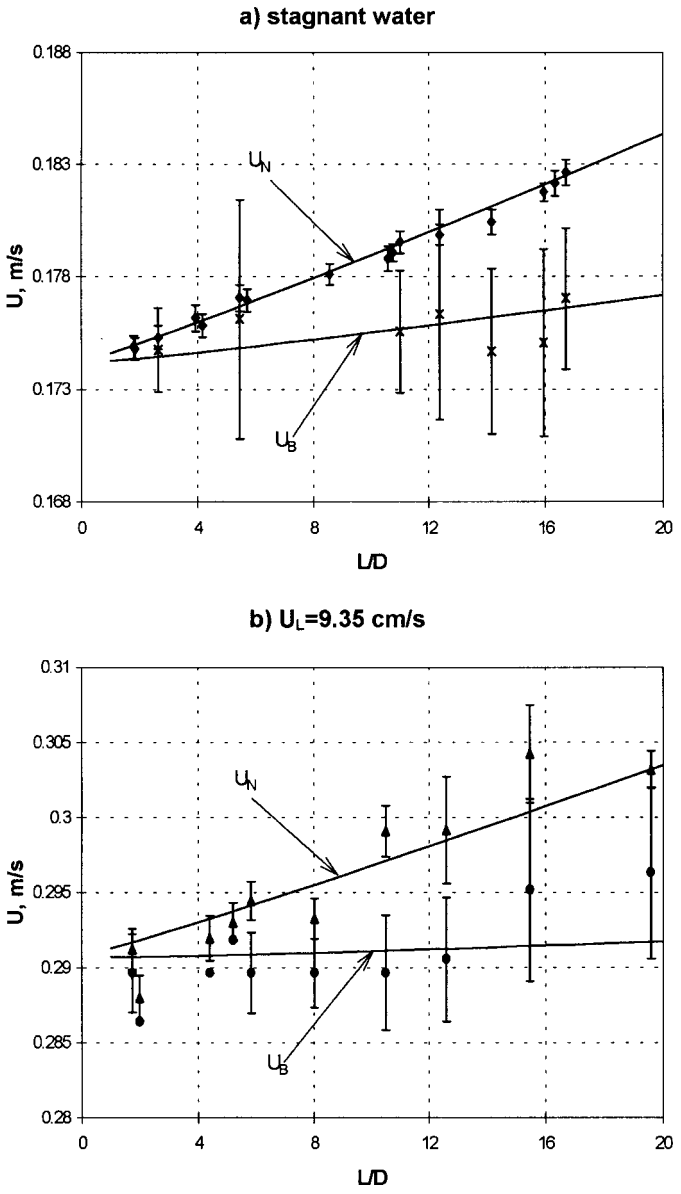

Fig. 7. Bubble nose and bottom velocities: (a) stagnant liquid; (b) $U_L = 9.35$ cm/s (points denote experimental data, solid lines—model).

and

$$U_N(h) = (CU_L + U_0)\left[1 - C\frac{\int_0^L r^2(x)\,dx}{R^2[P_a/(\rho_L g) + h]}\right]^{-1} \tag{8}$$

where R is the pipe radius. The velocity of the bubble tail is

$$U_T = U_N - \frac{dL}{dt} \tag{9}$$

The rate of length change can be found from rate of volume change

$$\frac{dV_G}{dt} = \frac{dL}{dt}\pi r^2(L) \tag{10}$$

On the other hand,

$$\frac{dV_G}{dt} = \frac{dV_G}{dh}\frac{dh}{dt} = -U_N\frac{dV_G}{dh} \tag{11}$$

where

$$\frac{dV_G}{dh} = \frac{d}{dh}\left(\frac{m_G\mathcal{R}T}{P_a + \rho_L g h}\right) = -\frac{V_G}{P_a/(\rho_L g) + h} \tag{12}$$

Combining Eqs. (10)–(12) yields

$$\frac{dL}{dt} = \frac{U_N\int_0^L r^2(x)\,dx}{r^2(L)[P_a/(\rho_L g) + h]} \tag{13}$$

and

$$U_T = U_N - \frac{dL}{dt} = U_N\left(1 - \frac{\int_0^L r^2(x)\,dx}{r^2(L)[P_a/(\rho_L g) + h]}\right) \tag{14}$$

The shape of the bubble $r(x)$ is taken from the experiment (Fig. 5). The values of U_N and U_T, calculated according to Eqs. (8) and (14) are also presented in Fig. 7. The model and the experimental results compare favorably.

3.3. Oscillations of the bubble bottom

As has been demonstrated in Fig. 3, the bubble bottom, in contrast to the bubble nose, does not retain a permanent shape while moving along the pipe. These variations in the instantaneous bubble bottom shape become more pronounced with increasing the bubble length. For longer bubbles, the sloshing anti-symmetric nature of the bubble bottom oscillation can clearly be observed in the experimental facility even by naked eye. The processing of the video images (cf. Fig. 3) corroborates this observation. The quasi-periodic character of these oscillations is evident in this figure. This well-organized pattern suggests the application of the Fourier analysis in order to describe this movement quantitatively. The total duration of the continuous record of a single bubble puts a limit on the frequency resolution that can be attained. In the present experiments, the bubble remains in the combined field of view of the two cameras for more than 2 s for the stagnant liquid experiments, so that the frequency resolution is better than about 0.5 Hz. The resolution is reduced for up-flowing liquid, and is limited to about 1 Hz for the case of the maximum liquid velocity.

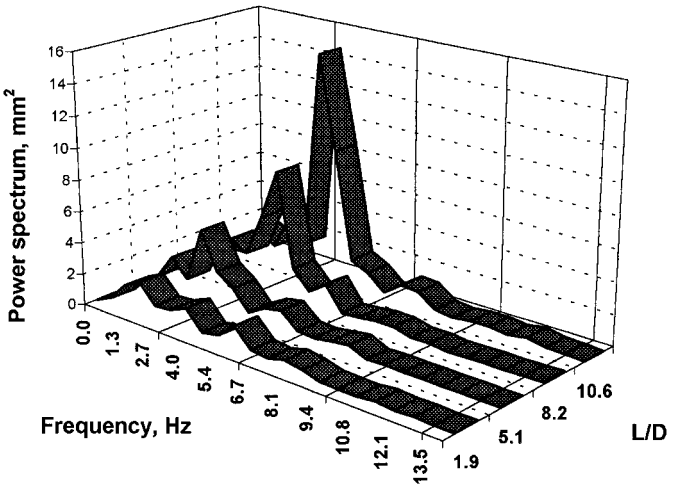

Fig. 8. Spectra of bubble bottom oscillations.

Power spectra of the bubble tail oscillations in stagnant liquid are presented in Fig. 8 for a number of bubble lengths. The spectra presented in this figure are averaged over few radial positions for each bubble, and then for a number of bubbles of similar length. The resonant character of the spectra is clearly seen, and the dominant frequency of the oscillations can be easily identified. Usually the averaging procedure is performed over about 10 radial positions and about five individual bubbles. The amplitude of the bubble oscillations is apparently growing with the bubble length, while the dependence of the frequency of those oscillation on the bubble length is less pronounced.

The accumulated data on the amplitude of the bubble bottom oscillations is presented in Fig. 9a, where the total energy, calculated as the integral of the power spectrum (cf. Table 1), is shown as a function of the bubble length for various liquid flow rates. The lines in this figure represent the linear best fit. For each liquid flow rate, the oscillations energy appears to increase with the bubble length. For any given bubble length, the oscillations energy increases with the liquid flow rate. Note that the axis of the sloshing motion has no preferred direction. The apparent amplitude of oscillations depends therefore on the cosine of the angle between the plane of observation and the random instantaneous direction of the axis of the sloshing motion. This phenomenon contributes to a considerable scatter observed in Fig. 9a.

The measured values of the dominant frequency of those oscillations are summarized in Fig. 9b. The dominant frequency seems to be essentially independent of the liquid flow rate. It increases somewhat with the bubble length, and seems to remain constant for longer bubbles. In most cases, the dominant frequency is about 4 Hz, and it does not exceed 5 Hz.

The salient resonant character of the measured spectra of the bubble bottom oscillations invites an attempt to calculate theoretically the resonant frequency. In the simplest approach, the movement of the bubble bottom can be modeled as that of a gas–liquid interface in a cylindrical container. Similar sloshing movement of the liquid surface can easily be observed in a glass of water after it has been declined. In the frame of reference moving with the bubble bottom, such standing wave on the free surface can be described in a linear approximation

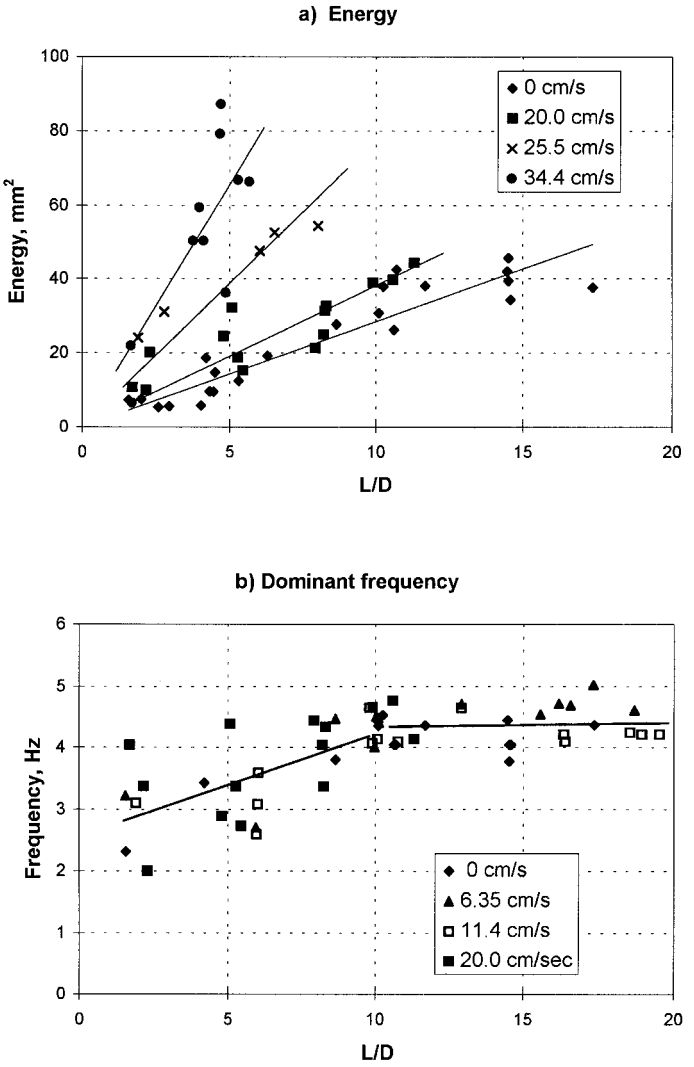

Fig. 9. Characteristics of the bubble bottom oscillations for various liquid velocities: (a) energy; (b) dominant frequency.

using the potential flow theory. The general solution of the Laplace equation for the velocity potential Φ in cylindrical coordinates (r, θ, z)

$$\nabla^2\Phi = 0 \tag{15}$$

is

$$\Phi(r, \theta, z, t) = A_s J_s(kr) e^{kz+i(\sigma t+\epsilon)} \tag{16}$$

where σ is the frequency of oscillations, k is the wave number and ϵ is the arbitrary phase angle. In Eq. (16), J_s is the Bessel function with the index s, and A_s is the arbitrary amplitude of the oscillations (Abramowitz and Stegun, 1964). The standard linearized kinematic and dynamic boundary conditions at the free surface can be written as

$$\frac{\partial \xi}{\partial t} = -\left.\frac{\partial \Phi}{\partial z}\right|_{z=0} \tag{17}$$

$$\frac{\partial \Phi}{\partial t} - gz = -\frac{T}{\rho}\left(\frac{1}{R_1} + \frac{1}{R_2}\right) \tag{18}$$

where ξ is the instantaneous surface elevation, R_1 and R_2 are the principal radii of curvature, and T is the surface tension coefficient. This leads to the well-known dispersion relation for gravity-capillary waves

$$\sigma^2 = gk + \frac{T}{\rho}k^3 \tag{19}$$

Assuming that the radial velocity on the bubble circumference is zero (rigid boundary):

$$\left.\frac{\partial \Phi}{\partial r}\right|_{r=R} = 0 \tag{20}$$

the dominant lowest mode is obtained from the equation $J_1'(kR) = 0$. Note that the present derivation follows that of Lamb (1932) but takes into account the surface tension effects. For our pipe radius ($R = 12.5$ mm), Eqs. (19)–(20) yield a dominant first antisymmetric mode with a frequency of 6.5 Hz (applying Lamb's calculations without surface tension results in a slightly lower value of 6.05 Hz). The calculated dominant frequency is notably higher than the experimentally measured values in Fig. 9b. This discrepancy may result from a number of reasons. The crudest assumption, however, adopted in the simplified analysis is the non-penetrating boundary condition (Eq. (20)). Actually, the bubble is surrounded by a circular wall jet with velocities notably exceeding those of the moving bubble. Due to the complexity of this flow with an unknown free surface and a shear flow in the circular jet, an exact solution can not be easily obtained. As a result of the fact that the jet is capable of consuming the radial mass flux, nonzero radial velocity at $r = R$ exists. Hence, the more appropriate equation for the determination of the lowest eigenmode is

$$\left.\frac{\partial \Phi}{\partial r}\right|_{r=R} = \text{const.} \tag{20a}$$

so that $J_1'(kR) = B$, where B is in the range $0 < B < 0.5$, but its exact value cannot be specified. As a result of that, the wavelength of the standing wave, determined by the wavenumber k, may become significantly larger, corresponding to lower oscillation frequencies than those calculated from Eqs. (19) and (20), as observed in the experiments (Fig. 9b). For example, the choice of $B = 0.3$ corresponds to a dominant antisymmetric mode with a frequency of 4.75 Hz, close to the experimental observations.

The adopted simplified linear potential model can thus grasp only the general resonant character of the observed oscillations and explain the apparent independence of the resonant frequency on the bubble length and flow rate. It is, however, incapable of providing any information regarding the amplitude of those oscillations which is determined by the complicated shear flow in the circumference of the bubble. Both the bubble length and the liquid flow rate contribute to the increase in the shear stress in the liquid film. The growth of the energy of the resonant oscillations with these parameters (Fig. 9a) can thus be related to the shear stress in the film.

4. Conclusions

The propagation of a single elongated bubble in a vertical pipe can be seen as one of the fundamental flow patterns. It is thus of a basic scientific interest, beyond its importance for the analysis of two-phase slug flow. The behavior of the elongated bubble, as well as the flow field in the liquid surrounding the bubble are very complicated. Only a limited amount of publications considering either theoretical or experimental aspects of this flow can be found in the literature. The present study represents an attempt to attack this exciting hydrodynamic problem by performing quantitative measurements.

An experimental technique based on the digital processing of a continuous sequence of video images is developed. This technique enables to follow a single bubble over a considerable interval, thus allowing time-dependent characteristics of the bubble motion to be obtained. This technique makes it possible to detect minor variations in the instantaneous bubble shape.

New experimental results about the time-averaged parameters related to an elongated bubble motion in a vertical pipe are collected. Values of the coefficient C in Eq. (1) are obtained for various liquid flow rates. The generally accepted assumption that the value of C is related to the shape of the velocity profile ahead of the bubble is extended here to the undeveloped flow in the entry region. This information is essential for modeling undeveloped slug flow. The bubble shape, as well as the dependence of the bubble propagation velocity on the bubble length due to compressibility effects, is obtained. These experimental results are in agreement with suggested physical models.

Particular attention is given in the present study to the investigation of the time-dependent characteristics of the Taylor bubble motion. A resonant character of the oscillations of the bubble bottom is demonstrated. The variation of the frequency spectra of these oscillations with the bubble length and the liquid velocity is studied. It is shown that, while the dominant frequency of the bubble bottom oscillations is nearly constant, their amplitude increases strongly with the bubble length as well as with the liquid velocity.

The detailed knowledge of the characteristics of the bubble bottom oscillations is a necessary step in the study of the velocity field in the Taylor bubble wake. The velocity distribution behind the Taylor bubble controls the acceleration of the ensuing Taylor bubble in an undeveloped slug flow. This information is therefore essential for the construction of accurate theoretical models for the prediction of complex slug flow behavior.

References

Abramowitz, M., Stegun, I.A., 1964. Handbook of Mathematical Functions. Dover, New York.
Barnea, D., 1990. Effect of bubble shape on pressure drop calculations in vertical slug flow. Int. J. Multiphase Flow 16, 79–89.
Barnea, D., Brauner, N., 1985. Hold-up of the liquid slug in two phase intermittent flow. Int. J. Multiphase Flow 11, 43–49.
Barnea, D., Taitel, Y., 1993. A model for slug length distribution in gas liquid slug flow. Int. J. Multiphase Flow 19, 829–838.
Campos, J.B.L.M., Guedes de Carvalho, J.R.F., 1988a. An experimental study of the wake of gas slugs rising in liquids. J. Fluid Mech. 196, 27–37.
Campos, J.B.L.M., Guedes de Carvalho, J.R.F., 1988b. Mixing induced by air slugs rising in narrow columns of water. Chem. Engng Sci. 43, 1569–1582.
Collins, R., de Moraes, F.F., Davidson, J.F., Harrison, D., 1978. The motion of a large gas bubble rising through liquid flowing in a tube. J. Fluid Mech. 89, 497–514.
Davies, R.M., Taylor, G.I., 1949. The mechanics of large bubbles rising through extended liquids and through liquid in tubes. Proc. R. Soc. Lond. Ser. A 200, 375–390.
Dumitrescu, D.T., 1943. Stromung an einer Luftblase im senkrechten Rohr. Z. Angew. Math. Mech. 23, 139–149.
Goldsmith, H.L., Mason, S.G., 1962. The movement of single large bubbles in closed vertical tubes. J. Fluid Mech. 14, 52–58.
Kvernvold, O., Vindoy, V., Sontvedt, T., Saasen, A., Selmen-Olsen, S., 1984. Velocity distribution in horizontal slug flow. Int. J. Multiphase Flow 10, 441–457.
Lamb, H., 1932. Hydrodynamics, article 191. Cambridge University Press, Cambridge pp. 284–290.
Mao, Z-S., Dukler, A., 1990. The motion of Taylor bubbles in vertical tubes: I. A numerical simulation for the shape and rise velocity of Taylor bubbles in stagnant and flowing liquid. J. Comput. Phys. 91, 132–160.
Mao, Z-S., Dukler, A., 1991. The motion of Taylor bubbles in vertical tubes: II. Experimental data and simulations for laminar and turbulent flow. Chem. Engng Sci. 46, 2055–2064.
Moissis, D., Griffith, P., 1962. Entrance effects in a two-phase slug flow. J. Heat Transfer, Trans. ASME, Ser. C 2, 29–39.
Nakoryakov, V.E., Kashinsky, O.N., Petukhov, A.V., Gorelik, R.S., 1989. Study of local hydrodynamic characteristics of upward slug flow. Exp. Fluids 7, 560–566.
Nicklin, D.J., 1962. Two-phase bubble flow. Chem. Engng Sci. 17, 693–702.
Nicklin, D.J., Wilkes, J.O., Davidson, J.F., 1962. Two-phase flow in vertical tubes. Trans. Inst. Chem. Engng 40, 61–68.
Pinto, A.M.F.R., Campos, J.B.L.M., 1996. Coalescence of two gas slugs rising in a vertical column of liquid. Int. J. Multiphase Flow 51, 45–54.
Pratt, W.K., 1978. Digital Image Processing. Wiley, New York.
Shemer, L., Barnea, D., 1987. Visualization of the instantaneous velocity profiles in gas-liquid slug flow. Physicochem. Hydrodyn. 8, 243–253.
Taitel, Y., Barnea, D., 1990. Two-phase slug flow. Adv. Heat Transfer 20, 83–132.
Taitel, Y., Barnea, D., Dukler, A.E., 1980. Modeling flow pattern transitions for steady upward gas–liquid flow in vertical tubes. AIChE J. 26, 345–354.
White, E.T., Beardmore, R.H., 1962. The velocity of rise of single cylindrical air bubbles through liquids contained in vertical tubes. Chem. Engng Sci. 17, 351–361.
White, F.M., 1986. Fluid Mechanics. McGraw-Hill, New York.
Zukoski, E.E., 1966. Influence of viscosity, surface tension, and inclination angle on motion of long bubbles in closed tubes. J. Fluid. Mech. 25, 821–837.